Soft magnetism in single phase Fe_3Si thin films deposited on $SrTiO_3(001)$ by pulsed laser deposition

Icíar Arnay[1,2,3], Aída Serrano[1,2,4], Verónica Braza[5], Rosalía Cid[1,2,6], Ana M. Sánchez[7], Jesús López-Sánchez[1,2], Germán R. Castro[1,2], Juan Rubio-Zuazo[1,2]*

1. Spanish CRG BM25-SpLine at The European Synchrotron. 71 Av. des Martyrs 38000 Grenoble, France
2. Instituto de Ciencia de Materiales de Madrid, CSIC, C/Sor Juana Inés de la Cruz 3, 28049 Madrid, Spain
3. IMDEA Nanociencia C/Faraday 9, 28049 Madrid, Spain
4. Instituto de Cerámica y Vidrio, CSIC, C/Kelsen 5, 28049 Madrid, Spain
5. Instituto de Microscopía Electrónica y Materiales (IMEYMAT) Universidad de Cádiz, Facultad de Ciencias, 11510 Puerto Real, Cádiz, Spain
6. CIC EnergiGUNE, Parque Tecnológico de Álava, Albert Einstein, 48, 01510 Vitoria-Gasteiz, Spain
7. Department of Physics, University of Warwick, Coventry CV4 7AL, United Kingdom

**Corresponding author: I. Arnay (current address: IMDEA Nanociencia C/Faraday 9, 28945 Madrid, iciar.arnay@imdea.org)*

Abstract: *The development of devices relying on spin phenomena requires of an ideal spin polarized electron source. This can be achieved by taking advantage of half-metallic full Heusler alloy thin films. However, their implementation requires a controlled growth of stoichiometric films with large activation volumes. In this work, we report on the growth of epitaxial Fe_3Si ultra-thin films by pulsed laser deposition on $SrTiO_3(001)$ substrates, analyzing the effect of deposition temperature in the structural, morphological and magnetic properties of the deposited films. We conclude that optimal compromise between phase purity and interface quality is obtained at 200 ºC, obtaining the best magnetic response under this condition.*

Keywords: crystal growth, half-metal, transmission electron microscopy (TEM), synchrotron radiation, magnetic measurements

Graphical abstract

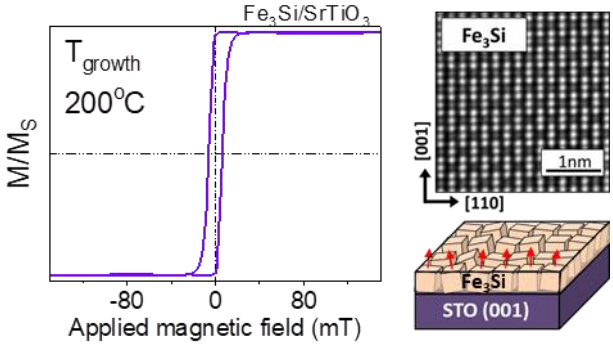

1. Introduction

Heusler alloys are characterized by a face centered cubic superlattice with a body centered cubic unit cell. This particular structure allows to explore novel properties of materials not found in their pure state, as it is the case, for instance, of the first discovered alloy, Cu_2MnSn, which shows ferromagnetism although none of the constituent elements are ferromagnetic in its elemental state [1]. In 1983, Groot et al. predicted the half metallicity of NiMnSb at room temperature (RT)[2], which was experimentally confirmed a few years later by means of positron annihilation in bulk NiMnSb crystals [3]. In the following years, half metallicity has been reported in a large number of alloys [4,5], even in its thin film form [6], making them highly promising materials for the design of spin based devices [7,8]. Fe_3Si is part of this wide family of compounds, presenting a binary DO_3 structure with a lattice parameter of 5.65 Å. Fe_3Si presents ferromagnetic behavior up to 840 K, which provides a ferromagnetic response wide above RT, and it is characterized by a soft magnetism, with coercive fields in the order of few mT, and a low damping constant, which make it a great alternative for common ferromagnetic electrodes as permalloy for the study of spin based phenomena [9,10]. Tao *et al.* predicted the half metallic nature of Fe_3Si electrodes by modeling spin polarized transport through a MgO barrier [11]. However, they observed a strong dependence of spin polarization on the structural properties, with a dramatic reduction of the tunneling magnetoresistance (TMR) ratio due to interface oxidation. Also, a recent work by Xie *et al.* demonstrated a critical dependence of the electronic and magnetic properties on the degree of structural order [12]. Thus, the preparation of high quality films as well as a thoughtful characterization of their structural properties becomes mandatory. Although experimental reports are scarce, spin accumulation in a Si channel has been proved at low temperature in a lateral four-probe geometry using Fe_3Si/Si contacts [13]. The lack of experimental observations is related with the difficulty of stabilizing single-phase Fe_3Si films, which impedes the exploitation of its full potential.

Fe_3Si is usually grown by co-evaporation of Fe and Si in a contamination free ultrahigh vacuum (UHV) atmosphere, to obtain an accurate control of its stoichiometry [14-17]. On the contrary,

Fe_3Si preparation by pulsed laser deposition (PLD) is less frequent and to the author´s knowledge, only Yoshitake *et al.* have reported the preparation of polycrystalline Fe_3Si films on Si and quartz substrates using a Fe_3Si target [18], meanwhile no reports on epitaxial Fe_3Si films by PLD have been found. The most common substrate used for the preparation of Fe_3Si has been GaAs due to the similarity between their lattice parameter and lattice structure [14-15,19]. However, this similarity can also favor inter-diffusion processes and chemical exchange in the regions close to the interface [16]. Promising attempts have also been made on MgO, although the bigger lattice mismatch [17], as well as in other important semiconductors as Si [20]. Nevertheless, to the author´s best knowledge, there are no reports of $Fe_3Si/SrTiO_3$ systems. $SrTiO_3$ (STO) has attracted great attention itself due to its interesting optical and insulating properties, and as template for thin film growth by inducing new phenomena at the interface, as it is the formation of a two-dimensional electron gas on $LaAlO_3/SrTiO_3$ interface [21,22]. Moreover, STO, with a lattice constant of 3.905 Å, presents good lattice compatibility with a large number of functional materials as $La_{0.7}Sr_{0.3}MnO_3$ [23,24], $BaTiO_3$ [25,26] or $LaAlO_3$ [27,28]. Therefore, the integration of Fe_3Si on STO, opens the possibility for multifunctional spin-based systems design. Additionally, from Tao *et al.*, half metal behavior is related with the presence of tetragonal Fe_3Si lattice with a compressive in plane strain above the 1.3% (c/a>1.04) [12]. A commensurate growth on STO will fulfill this condition, so that only majority spin states should be present at the Fermi level for Fe_3Si/STO systems.

2. Experimental methods

Fe3Si thin films were deposited by PLD using an stoichiometric Fe3Si target. The laser was swept on the target to avoid the formation of craters and to minimize the emission of large particles. The target-to-sample distance was fixed to 50 mm and the offset between the sample and plume centers was set to 5 mm. A Nd:YAG laser with a wavelength of 355 nm, a pulse length of 9 ns, an energy per pulse of 280 mJ and a frequency of 10 Hz was used. Films were deposited on STO(001) substrates under UHV (1e-9mbar) conditions and at different substrate temperatures, exploring a range between 200 and 600 ºC. Fe3Si films with a nominal thickness of 20 nm were

evaporated with a rate of 0.46 nm/cycle. The epitaxial growth of the films was in-situ monitored by reflected high energy electron diffraction (RHEED). The equipment is situated at the BM25-SpLine support laboratory.Synchrotron-based X-ray diffraction (XRD), X-ray reflectivity (XRR) and X-ray absorption spectroscopy (XAS) measurements were performed at the BM25-SpLine beamline at The European Synchrotron (ESRF) in France. Crystallinity and morphology of the films was evaluated by XRD and XRR respectively, using a photon energy of 20 keV (λ=0.62 nm). XAS experiments were performed at the Fe K-edge (7112 eV) and analyzed following standard procedures using the Athena program [29,30]. Both X-ray absorption near edge structure (XANES) and Extended X-ray absorption fine structure (EXAFS) measurements were carried out in fluorescence mode at room temperature. Single crystal Fe_3Si and Fe foil standards were also studied. Specifically, EXAFS calculations were carried out using the FEFFIT code [29,30]. The Fourier transform (FT) was performed in the $k^3\chi(k)$ weighted EXAFS signal between 2.6 and 10.5 $Å^{-1}$. Experimental EXAFS results are fitted in R-space in the range 1.5-3 Å. The fitting was performed using the interatomic distance R and the Debye-Waller (DW) factors σ^2 as free parameters. The shift at the edge energy E_0 and the coordination number N were fixed. For all cases, a shell produced by the interaction of a Fe absorbing atom with eight Fe atoms and a shell from a Fe absorbing atom with six Fe/Si atoms are considered.

Scanning transmission electron microscopy (STEM) images were performed in IMEYMAT in Cádiz (Spain), using a Talos F200X microscope operated at 200 kV and department of physic in Warwick (United Kingdom) using Jeol ARM 200F with double aberration correction. Energy dispersive X-ray spectroscopy (EDX) analysis were obtained by using ChemiSTEM® technology with four integrated Bruker SDD detectors and processed using Velox® software.. The magnetic response of the samples was studied by longitudinal magneto optical Kerr effect *(*L-MOKE) using a home-made set-up at room temperature and ambient pressure.

3. Results and discussion

The crystallographic structure of the films was characterized by ex-situ XRD, recording a large number of reflections in order to determine epitaxial relations and to quantify lattice parameters and strain of the Fe_3Si lattice as a function of deposition temperature. Crystal truncation rods are shown in Fig. 1 along the STO(00L) (Fig. 1a) and STO(11L) (Fig. 1b) reciprocal space directions. An incommensurate growth of the Fe_3Si films on STO is evidenced by the presence of film peaks in non-integer positions of the reciprocal space, as shown in Fig. 1c and Fig. S1 (see Supporting Information, SI), with films presenting a bulk like lattice parameter within the experimental error (Table S1, see SI).. In order to optimize the coupling between Fe_3Si (a=5.695 Å) and STO (a=3.905 Å) lattices a 45 degrees in plane rotation occurs so that the following epitaxial relations are found: $Fe_3Si[001]||STO[001]$ and $Fe_3Si[100]||STO[110]$, regardless of the deposited temperature used. This configuration reduces the lattice mismatch from 31% ($100\%*(a_{Fe3Si}-a_{STO})/a_{STO}$), for an axis on axis growth, to 2% ($100\%*(a_{Fe3Si}-\sqrt{2}a_{STO})/\sqrt{2}a_{STO}$). As temperature is increased during growth, a progressive rise of intensity is observed. (001)-oriented Fe clusters formation is suspected by the asymmetric line shape of the Fe_3Si reflections for sample grew at 400 ºC and confirmed for sample deposited at 600 ºC.

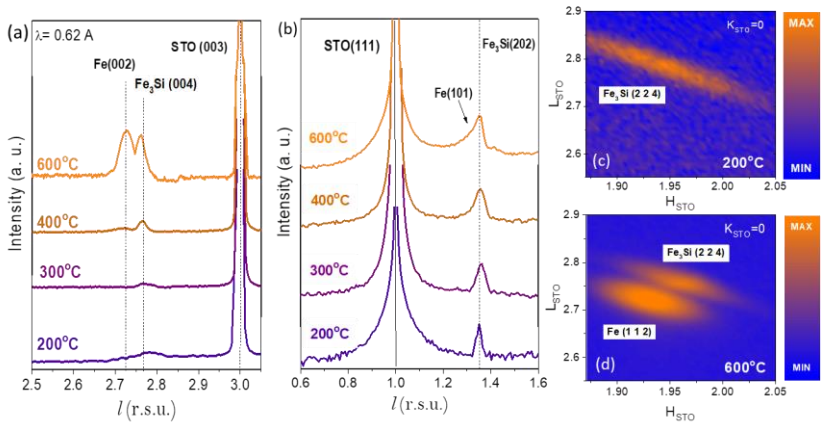

Fig. 1. XRD characterization of Fe_3Si/STO systems prepared by PLD. To the left, (a) [00L] and (b) [11L] rods recorded for different growth temperatures. To the right, reciprocal space maps recorded around Fe_3Si[224] reflection for samples deposited at (c) 200 ºC and (d) 600 ºC.

Reciprocal space maps (RSM) crossing $Fe_3Si(224)$ reflection are shown in Fig. 1c and Fig. 1d for samples deposited at 200 ºC and 600 ºC, respectively. For film deposited at 200 ºC the $Fe_3Si(224)$ reflection presents an elongated profile, which is characteristic of a high degree of mosaicity, i.e. indicates the presence of slightly tilted domains respect to the STO[001] axis. This profile is also characteristic for samples deposited at 300 ºC and 400 ºC (see SI). A significant improvement of the crystallinity is observed when increasing deposition temperature up to 600 ºC (Fig. 1a) in terms of higher diffraction intensities. Nevertheless, at this stage a second reflection is resolved, corresponding to the presence of 001-oriented Fe clusters, coupled axis on axis with the Fe_3Si lattice, as evidenced in the recorded rods (Fig. 1a and b) and RSM (Fig. 1d). Thickness and surface roughness was evaluated by synchrotron based X-ray reflectivity measurements. A progressive increase of the roughness is observed as deposition temperature increases, which is demonstrated by a faster decay of the reflected intensity as well as a faster attenuation of the Kiessig fringes amplitude with increasing incident angle (see SI). The transition from a stripe like to a dot like pattern in RHEED pattern also evidences roughness increase and could be related to a transition from a 2D to a 3D growth (Fig. S2.a).

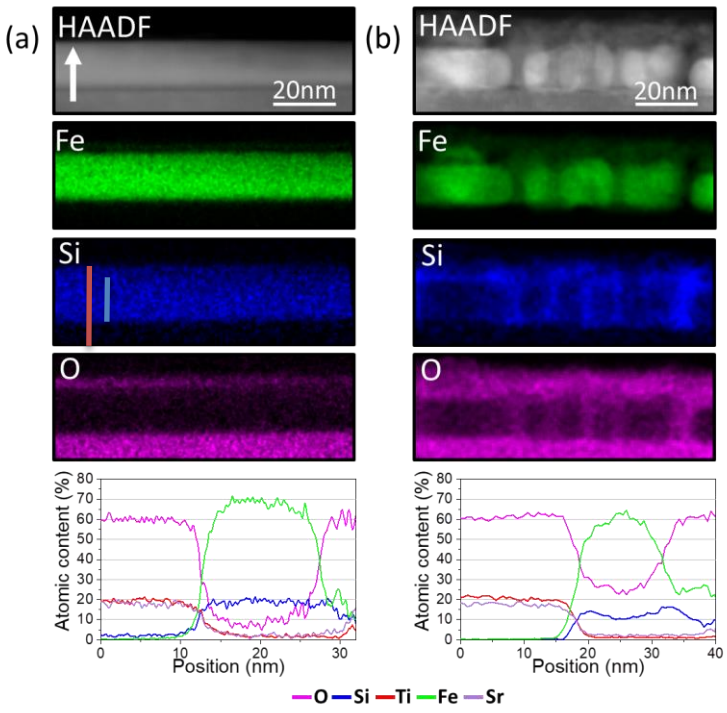

Fig. 2. From top to bottom HAADF-TEM image and element selective EDX measurements in the same region for Fe-K, Si-K and O-K edges and composition profile along growth direction marked by white arrow for Fe_3Si films grown at (a) 200 ºC and (b) 600 ºC.

Insight information about sample homogeneity and local structure was obtained by combined STEM and EDX analysis. Fig. 2 shows high angle annular dark field (HAADF) images as well as element selective EDX measurements for Fe-K, Si-K and O-K edges for films grown at 200 ºC (Fig. 2a) and 600 ºC (Fig. 2b) along growth direction. The morphology of the samples shows a clear dependence with the deposition temperature. The film deposited at 200 ºC presents a planar morphology with a homogeneous thickness of the Fe_3Si layer averaging 14 nm, in agreement with RHEED and XRR results (Fig. S2). EDX characterization indicates a homogeneous 3:1 Fe:Si ratio corroborating the stoichiometric growth of Fe_3Si phase at this temperature. Element selective characterization shows a very low segregation of elements from the substrate to the layer, observing a transition zone of a few nanometers. Oxygen decreases drastically in the layer of interest, showing a low content probably due to surface oxidation. For samples deposited at 600 ºC HAADF images indicate the formation of a discontinuous film, consisting of clusters with similar heights ranging between 12 and 15 nm, evidencing a transition from 2D to 3D growth as already intuited by *in situ* RHEED characterization (see SI). EDX analysis shows an uneven distribution of Fe and Si along the film. Element selective characterization evidences the presence of clusters consisting of pure Fe as well as stoichiometric Fe_3Si (Fig. S3). Meanwhile, inter-grain areas are mainly formed by silicon containing oxides, as indicated by the high concentration of oxygen (Fig. 2). For samples prepared at intermediate temperatures, a progressive transition from the features shown at 200 ºC and 600 ºC is identified in accordance with the XRD (Fig. 1) and XRR (Fig. S2) results.

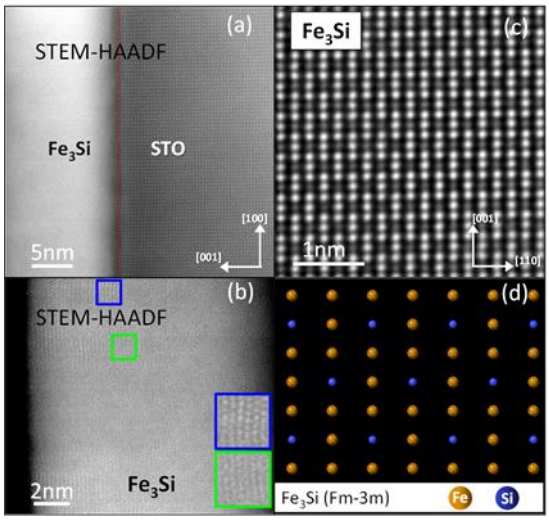

Fig. 3. STEM characterization of Fe_3Si films deposited at 200 ºC on STO(001). (a) High magnification STEM-HAADF at the Fe_3Si/STO interface, along STO[100] (The red line indicates the beginning of the transition layer formed in the intermediate layer) (b) High magnification STEM-HAADF in the layer of interest and enlargement of the two regions marked with green and blue squares. (c) Atomic resolution image of the layer of interests corresponding to [110]Fe_3Si projection, confirming 45 degrees in plane rotation. (d) Schematic of the Fe_3Si [Fm-3m] structure in a [110] projection.

Fig. 3 shows high magnification STEM-HAADF images of the Fe_3Si/STO interface for the film grown at 200 ºC. Here, a low crystallinity transition layer with a thickness of about 2 nm is observed, in accordance with EDX. Figure 3a shows this darker transition layer with respect to the substrate and the layer of interest, which is marked with a red line its beginning. More likely, this transition layer allows the relaxation of the Fe_3Si lattice resulting in a bulk-like cubic structure. Atomic resolution image show Fe_3Si[100]||STO[110] with different regions atomically resolved to different degrees. Fig. 3b shows areas where atoms have been resolved (blue box) and others where lines ore observed (green box). These slight differences are hard to see, so one way to observe them more clearly is by using the Fast Fourier Transform (FFT). For this purpose, FFTs have been performed on different regions of the sample. In fig.4 it can be seen how for the film grown at the lowest temperature (200 ºC), the FFTs of the two selected regions are tilted to different degrees respect to vertically drawn yellow line. Indeed, if we focus on the spots closer to the yellow line, we can see how they move further away from this line in a zone (red box) with respect other one (blue box). This is due to the presence of domains slightly inclined concerning

the axis of the substrate zone, as well as between them, which confirms the mosaic character of the film, as supported by the XRD results (Fig.1).

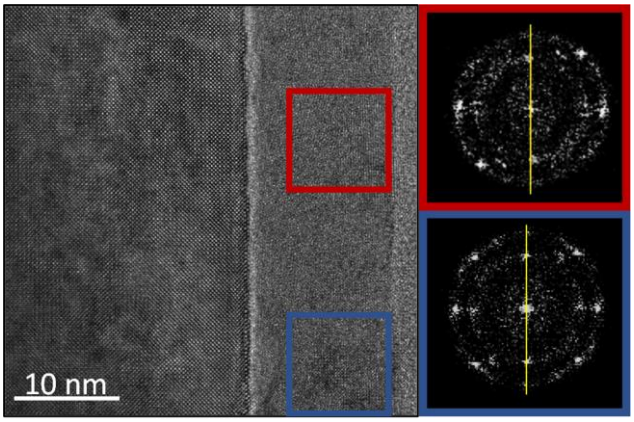

Fig. 4. High magnification STEM-HAADF and FFT of two regions marked with the red and blue boxes for the sample deposited at 200 ºC.

In order to analyze some possible amorphous phases and the short-range order of films as a function of the deposition temperature, XAS characterization was followed. Fig. 5a shows the XANES spectra for the prepared films as well as those recorded for single crystal Fe_3Si and Fe foil standards. For all films, the average valence was calculated to be 0 from the absorption edge position taking the first maximum in the first derivative of the XANES spectra [31,32] and no evidences of oxide Fe is identified varying the deposition temperature. The compositional character of the films is reflected in the XANES curves. Films prepared at 200 ºC and 300 ºC show a XANES signal similar to that of the Fe_3Si reference, although with lower intensity in the resonances. From 400 ºC onwards, the appearance of new resonances in the absorption signal is observed in the XANES spectrum with similarities to that of the Fe reference. Similar behavior has been observed in $Fe_{73.9}Cu_1Nb_3Si_{15.5}B_{6.6}$ ribbons with the ball milling time [33]. An estimation of the average Fe:Fe_3Si ratio in the average volume of the samples was carried out by means of a linear combination fitting (LCF) using the Fe_3Si and Fe references. Quantitative results are shown in Fig. 5b, showing the apparition of Fe phase at 400 ºC with a significant Fe:Fe_3Si ratio of around 1:3. The ratio is enhanced to 3:1 for the film grown at 600 ºC. These results corroborate those obtained from XRD (Fig. 1) and TEM (Fig. 2) experiments and the influence of the deposition temperature in the growth process of Fe_3Si epitaxial thin films.

Fig. 5c displays the modulus of the FT of the EXAFS signal at the Fe K-edge for all samples along with those of the Fe foil and the Fe_3Si single crystal. Numerical EXAFS results are presented in the Table I.

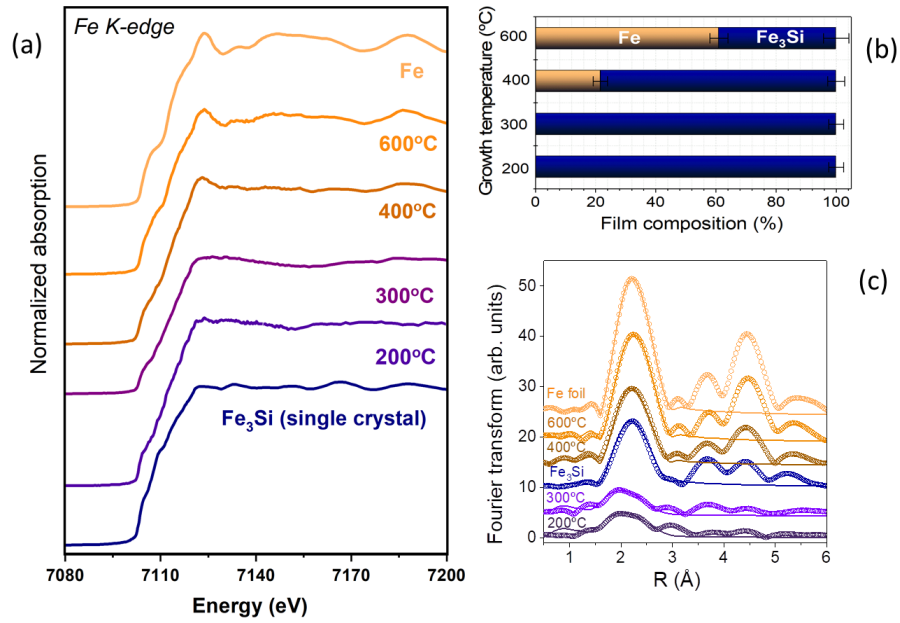

Fig. 5. XAS characterization of Fe_3Si thin films deposited at different temperatures. a) XANES spectra at the Fe K-edge for samples deposited at 200, 300, 400 and 600 ºC together with Fe_3Si single crystal and Fe foil references. b) Phase composition in weight fraction extracted from linear combination fitting of XANES spectra for different samples. c) FT modulus of the EXAFS spectra (points) at the Fe K-edge and best-fitting simulations (continuous lines) for the different samples.

Table I. Results of the EXAFS fittings for the first and second shells of films at Fe K-absorption edge. *R*: interatomic distance and DW: Debye-Waller factor.

Sample	**Shell**	**R (Å)**	**DW(Å^2)**
Fe foil	Fe-Fe	2.476(5)	0.007(1)
	Fe-Fe	2.816(8)	0.010(2)
Fe_3Si single crystal	Fe-Fe	2.444(3)	0.003(1)
	Fe-Si	2.774(6)	0.009(1)
600 ºC	Fe-Fe	2.475(3)	0.006(1)
	Fe-Fe/Si	2.810(5)	0.010(1)
400 ºC	Fe-Fe	2.468(4)	0.006(1)
	Fe-Fe/Si	2.804(8)	0.010(1)
300 ºC	Fe-Fe	2.325(3)	0.003(1)

	Fe-Si	2.825(4)	0.003(1)
200 ºC	Fe-Fe	2.320(7)	0.003(1)
	Fe-Si	2.825(6)	0.003(1)

From the analysis of the Fe K-edge EXAFS signal of films grown at 400 and 600 ºC, the first shell is located around 2.47 Å and is associated with the distances between Fe atoms (Fe-Fe bonds) while the second shell around 2.80 Å is related to the distances between Fe and Fe/Si atoms (Fe-Fe/Si bonds). Both distances fall between those of the Fe foil and the Fe_3Si single crystal, indicating the coexistence of both phases especially for the film with highest deposition temperature. The films with deposition temperature of 200 and 300 ºC show a different EXAFS behavior as compared to the films deposited at high temperatures. Both samples show a clear decrease of the intensity and a shift of the first neighbor position, with the first shell around 2.32 Å and the second one around 2.82 Å (see Table 1). These findings could be attributed to the mosaicity and consequent to some extent misorientation that occurs in a short range for films prepared at lowest deposition temperature, as identified above.

With respect to the evolution of the DW factors, films prepared at 400 and 600 ºC present values between those of Fe foil and Fe_3Si single crystal while films obtained at the lowest deposition temperature show smaller DW factors indicating a reduction of the structural disorder of Fe_3Si films (see Table I). This is most likely related with the high mosacity of the samples in this temperature range, which allows the complete relaxation of the lattice.

The loss of the single phase character of the films with the deposition temperature is clearly evidenced in the modification of the magnetic response. Fig. 6 shows normalized hysteresis loops recorded at RT and ambient pressure as a function of deposition temperature as well as the evolution of the coercive field (H_C) and normalized remanent magnetization (M_R/M_S). Stoichiometric films deposited at 200 and 300 ºC present low coercive fields (H_C<10 mT) and high remanence (M_R/M_S~1 and ~0.9 for film grown at 200 ºC and 300 ºC, respectively). These values are in good agreement with previous observations in epitaxial Fe_3Si/GaAs films prepared by co-deposition [34]. On the contrary, no uniaxial anisotropy is observed and the films present

equivalent hysteresis loops in all in-plane directions, more likely due to the rupture of long-range order due to mosaicity as indicated by XRD characterization. As the temperature increases during deposition, coercitivity increases and the remanence drops from 1 to almost 0.7.

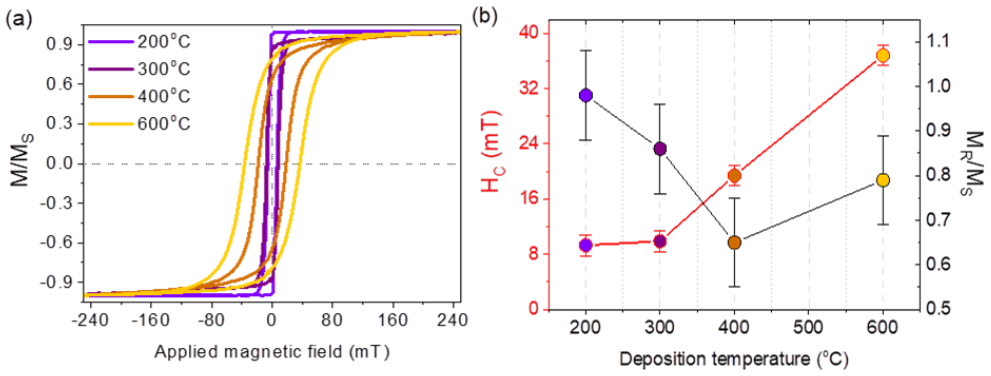

Fig. 6. L-MOKE characterization for Fe_3Si films deposited on STO(001) at different temperatures. a) Normalized hysteresis loops recorded as a function of deposition temperature and b) evolution of the coercive field (H_C) and normalized remanent magnetization (M_R/M_S).

This evolution is related to two simultaneous phenomena. First, the presence of Fe-clusters, which is known to result in higher coercive fields [27], and second the dramatic change in the morphology from a planar to a granular system (i.e., from 2D to 3D growth), as evidenced by high magnification STEM characterization. The presence of amorphous silicon oxide in between the magnetic Fe-Si islands (Fig. 2b) limits the inter-granular exchange, resulting in smooth hysteresis curves, as observed for other granular systems [35]. Also, the presence of different Fe:Si ratios in the different grains as well as variations in grain size induce a field dispersion in the single grain switching, which also contributes to the observation of a broad magnetic transition [36].

4. Conclusions

In this work we have explored different conditions for the deposition of half-metallic epitaxial Fe_3Si films on STO(001) substrates by PLD. Our results demonstrate a strong correlation between deposition temperature and the structural, compositional, morphological and magnetic properties

of the films. In order to obtain homogeneous, planar, stoichiometric and single phase Fe_3Si films with optimal magnetic response the temperature must be kept below 300 ºC during the deposition. In this temperature range, an homogeneous composition with a Fe:Si 3:1 ratio is proved by combination of local (EDX) and macroscopic (XAS) characterization. XRD and HR-TEM corroborate the 001-oriented epitaxial growth of the Fe_3Si phase, with 45 degrees in plane rotation respect to STO axis in order to minimize the misfit between both lattices. Under the mentioned conditions, Fe_3Si/STO films show very interesting structural and magnetic behavior, opening a promising new route for the integration of Fe_3Si in spin-based devices.

Acknowledgment

The authors are grateful to the BM25-SpLine Staff for their valuable help and for the financial support from the Spanish MCIN and Consejo Superior de Investigaciones Científicas [Grant No. 2010-6-OE-013 and 2021 60 E 030]. IA acknowledges support by the Community of Madrid (CM) through Project P2018/NMT4321 (NANOMAGCOST), by MINECO through Project RTI2018-097895-B-C42 (FUN-SOC), PCI2019-111867-2 (FLAG-ERA JTC 2019, SOgraphMEM), and by the "Severo Ochoa" Programme for Centres of Excellence in RD, MINECO grant SEV-2016-0686.. A.S. acknowledges the financial support from the Comunidad de Madrid for an "Atracción de Talento Investigador" contract (No. 2017-t2/IND5395).

References

[1] F. Heusler, Über magnetische manganlegierungen, Verh. Dtsch. Phys. Ges., 5 (1903), p. 219
[2]R. A. de Groot, F. M. Mueller, P. G. van Engen, and K. H. J. Buschow, New class of materials: Half-metallic ferromagnets, Phys. Rev. Lett 50 (1983) 2024-2027; https://doi.org/10.1103/PhysRevLett.50.2024
[3] K. E. H. M. Hanssen, P. E. Mijnarends, L. P. L. M. Rabou, and K. H. J. Buschow, Positron-annihilation study of the half-metallic ferromagnet NiMnSb: Experiment, Phys. Rev. B 42 (1990) 1533: https://doi.org/10.1103/PhysRevB.42.1533[4] X. J. Zhang, Z. H. Liu, Y. J. Zhang, H. Y. Liu, G. D. Liu, Y. T. Cui, X. Q. Ma, Theoretical and experimental study of the phase formation for Ti2YAl and Ti2Y` Ga (Y = Co, Fe; Y′ = Cr, Fe) Intermetallics 73 (2016) 26–30: https://doi.org/10.1016/j.intermet.2016.02.008
[5] L. Hongzhi, Z. Zhiyong, M. Li, X. Shifeng, L. Heyan, Q. Jingping, L. Yangxian, W. Guangheng, Electronic structure and magnetic properties of Fe_2YSi (Y = Cr, Mn, Fe, Co, Ni) Heusler alloys: a theoretical and experimental study, J. Phys. D: Appl. Phys. 40(22) (2007) 7121: https://doi.org/10.1088/0022-3727/40/22/039
[6] M. Jourdan, J. Minár, J. Braun, A. Kronenberg, S. Chadov, B. Balke, A. Gloskovskii, M. Kolbe, H.J. Elmers, G. Schönhense, H. Ebert, C. Felser, M. Kläui, Direct observation of half-metallicity in the Heusler compound Co_2MnSi, Nat.Comm. 5 (2014) 3974: https://doi.org/10.1038/ncomms4974
[7] K. Elphick, W. Frost, M. Samiepour, T. Kubot, K. Takanashi, Hiroaki Sukegawa, S. Mitani, and Atsufumi Hirohata, Heusler alloys for spintronic devices: review on recent development and future

perspectives, Science and technology advanced materials 22 (2021) 235-271; http://doi.org/10.1080/14686996.2020.1812364
[8] S. A. Khandy, I. Islam, D. C. Gupta and A. Laref, Full Heusler alloys (Co_2TaSi and Co_2TaGe) as potential spintronic materials with tunable band profiles, Journal of Solid State Chemistry 270, (2019) 173-179; https://doi.org/10.1016/j.jssc.2018.11.011
[9] W. Rotjanapittayakul, W.Pijitrojana, T. Archer, S. Sanvito, J. Prasongkit, Spin injection and magnetoresistance in MoS_2-based tunnel junctions using Fe_3Si Heusler alloy electrodes, Sci Rep 8 (2018) 4779: https://doi.org/10.1038/s41598-018-22910-9
[10] H. Y. Hung, G. Y. Luo, Y. C. Chiu, P. Chang, W. C. Lee, J. G. Lin, S. F. Lee, M. Hong, J. Kwo, Detection of inverse spin Hall effect in epitaxial ferromagnetic Fe_3Si films with normal metals Au and Pt, J.Appl. Phys. 113 (2013) 17C507: https://doi.org/10.1063/1.4799147
[11] L. L. Tao, S. H. Liang, D. P. Liu, H. X. Wei, Jian Wang, and X. F. Han, Tunneling magnetoresistance in Fe_3Si/MgO/Fe_3Si(001) magnetic tunnel junctions, Appl. Phys. Lett. 104 (2014) 172406; https://doi.org/10.1063/1.4874837
[12] J. Xie, Y.-F. Liao, D.-N. Wu, W.-J. Xiao, Q. Xie, The Degree-of-Order Dependent Electronic Structures and Magnetic Properties of Fe_3Si Alloys, Phys. Status Solidi B 257 (2020) 0370-1972; https://doi.org/10.1002/pssb.201900667
[13] Y. Ando, K. Hamaya, K. Kasahara, Y. Kishi, K. Ueda, K. Sawano, T. Sadoh, and M. Miyao, Electrical injection and detection of spin-polarized electrons in silicon through an Fe_3Si/Si Schottky tunnel barrier, Appl. Phys. Lett. 94 (2009) 182105; https://doi.org/10.1063/1.3130211
[14] J. Herfort, H. P. Schönherr, A. Kawaharazuka, M. Ramsteiner, K. H. Ploog, Epitaxial growth of Fe_3Si/GaAs(001) hybrid structures for spintronic application, J. Cryst. Growth 278 (2005) 666-670; https://doi.org/10.1016/j.jcrysgro.2004.12.124
[15] B. Jenichen, J. Herfort, U. Jahn, A. Trampert and H. Riechert, Epitaxial Fe_3Si/Ge/Fe_3Si thin film multilayers grown on GaAs(001), Thin Solid films 556 (2014) 120-124; https://doi.org/10.1016/j.tsf.2014.01.022
[16] C. Gusenbauer, T. Ashraf, J. Stangl, G. Hesser, T. Plach, A. Meingast, G. Kothleitner, and R. Koch, Interdiffusion in Heusler film epitaxy on GaAs(001), Phys Rev B 83 (2011) 035319; https://doi.org/10.1103/PhysRevB.83.035319
[17] Kh. Zakeri, I. Barsukov, N. K. Utochkina, F. M. Römer, J. Lindner, R. Meckenstock, U. von Hörsten, H. Wende, W. Keune, M. Farle, S. S. Kalarickal, K. Lenz, and Z. Frait, Magnetic properties of epitaxial Fe_3Si/MgO(001) thin films, Phys. Rev. B 76 (2007) 214421; https://doi.org/10.1103/PhysRevB.76.214421
[18] T. Yoshitake, D. Nakagauchi and K. Nagayama, Ferromagnetic Iron Silicide Thin Films Prepared by Pulsed-Laser Deposition, Jpn. J. Appl. Phys 42 (2003) L849;https://doi.org/10.1143/JJAP.42.L849
[19] S. Gaucher, B. Jenichen, J. Kalt, U. Jahn, A. Trampert, and J. Herfort, Growth of Fe_3Si/Ge/Fe_3Si trilayers on GaAs(001) using solid-phase epitaxy, Appl. Phys. Lett. 110 (2017) 102103; https://doi.org/10.1063/1.4977833
[20] T. Yoshitake, D. Nakagauchi, T. Ogawa, M. Itakura, N. Kuwano, and Y. Tomokiyo, Room-temperature epitaxial growth of ferromagnetic Fe_3Si films on Si(111) by facing target direct-current sputtering, Appl. Phys. Lett. 86 (2005) 262505; https://doi.org/10.1063/1.1978984
[21] D. Kan, T. Terashima, R. Kanda, A. Masuno, K. Tanaka, S. Chu, H. Kan, A. Ishizumi, Y. Kanemitsu, Y. Shimakawa and M. Takano, Blue-light emission at room temperature from Ar^+-irradiated SrTiO3, Nature Materials 4 (2005) 816; https://doi.org/10.1038/nmat1498
[22] J. Shen, H. Lee, R. Valentí, H. O. Jeschke, Ab initio study of the two-dimensional metallic state at the surface of $SrTiO_3$: Importance of oxygen vacancies, Phys. Rev. B 86 (2012) 195119; https://doi.org/10.1103/PhysRevB.86.195119
[23] F. Y. Bruno, J. Garcia-Barriocanal, M. Varela, N. M. Nemes, P. Thakur, J. C. Cezar, N. B. Brookes, A. Rivera-Calzada, M. Garcia-Hernandez, C. Leon, S. Okamoto, S. J. Pennycook, and J. Santamaria, Electronic and Magnetic Reconstructions in $La_{0.7}Sr_{0.3}MnO_3$/$SrTiO_3$ Heterostructures: A Case of Enhanced Interlayer Coupling Controlled by the Interface Phys. Rev. Lett. 106 (2011) 147205; https://doi.org/10.1103/PhysRevLett.106.147205
[24] J. Tornos, F. Gallego, S. Valencia, Y. H. Liu, V. Rouco, V. Lauter, R. Abrudan, C. Luo, H. Ryll, Q. Wang, D. Hernandez-Martin, G. Orfila, M. Cabero, F. Cuellar, D. Arias, F. J. Mompean, M. Garcia-Hernandez, F. Radu, T. R. Charlton, A. Rivera-Calzada, Z. Sefrioui, S. G. E. te Velthuis, C. Leon, and J. Santamaria, Ferroelectric Control of Interface Spin Filtering in Multiferroic Tunnel Junctions, Phys. Rev. Lett. 122 (2019) 037601; https://doi.org/10.1103/PhysRevLett.122.037601
[25] T. Q. Ngo, A. B. Posadas, M. D. McDaniel, C. Hu, J. Bruley, E. T. Yu, A. A. Demkov, and J. G. Ekerdt, Epitaxial c-axis oriented BaTiO3 thin films on $SrTiO_3$-buffered Si(001) by atomic layer deposition, Appl. Phys. Lett. 104 (2014) 082910; https://doi.org/10.1063/1.4867469

[26] A. Gómez, J. M. Vila-Fungueiriño, R. Moalla, G. Saint-Girons, J. Gázquez, M. Varela, R. Bachelet, M. Gich, F. Rivadulla, and A. Carretero-Genevrier, Electric and Mechanical Switching of Ferroelectric and Resistive States in Semiconducting $BaTiO_{3-\delta}$ Films on Silicon, Small, 13 (2017) 1701614; https://doi.org/10.1002/smll.201701614
[27] M. Scigaj, J. Gázquez, M. Varela, J. Fontcuberta, G. Herranz, F. Sánchez, Conducting interfaces between amorphous oxide layers and $SrTiO_3$(110) and $SrTiO_3$(111), Solid State Ionics 281 (2015) 68; https://doi.org/10.1016/j.ssi.2015.09.002
[28] H. Yan, J. M. Börgers, M.-A. Rose, C. Baeumer, B. Kim, L. Jin, R. Dittmann, and F. Gunkel, Stoichiometry and Termination Control of $LaAlO_3/SrTiO_3$ Bilayer Interfaces, Adv. Mater. Interfaces, 8 (2021) 2001477; https://doi.org/10.1002/admi.202001477
[29] B. Ravel and M. Newville, ATHENA, ARTEMIS, HEPHAESTUS: data analysis for X-ray absorption spectroscopy using IFEFFIT, J. Synchrotron Radiat., 12 (2005) 537−54; https://doi.org/10.1107/S0909049505012719
[30] M. Newville, IFEFFIT : interactive XAFS analysis and FEFF fitting, J. Synchrotron Radiat., 8, (2001) 322−324; https://doi.org/10.1107/S0909049500016964
[31] M. Abuín, A. Serrano, J. Chaboy, M. A. García, N. Carmona, XAS study of Mn, Fe and Cu as indicators of historical glass decay, J. Anal. At. Spectrom. 28 (2013) 1118−1124; https://doi.org/10.1039/C3JA30374H
32] J. Rubio-Zuazo, A. Chainani, M. Taguchi, D. Malterre, A. Serrano, G.R. Castro, Electronic structure of FeO, $\gamma-Fe_2O_3$, and Fe_3O_4 epitaxial films using high-energy spectroscopies, Phys. Rev. B, 97 (2018) 235148; https://link.aps.org/doi/10.1103/PhysRevB.97.235148
[33] J. Lopez-Sanchez, E. Navarro, A. Serrano, C. Granados-Millares, A. del Campo, A. Quesada and P. Marín, Ultrafast Particle Size Reduction of $Fe_{73.9}Si_{15.5}Cu_1Nb_3B_{6.6}$ by High-Energy Milling: Nb_2O_5 as a Marker of Permeability Enhancement and Magnetic Hardening, ACS Appl. Electron. Mater. 2, (2020)1484−1496; https://doi.org/10.1021/acsaelm.0c00252
[34] J. Herfort, H.-P. Schönherr, K.-J. Friedland, and K. H. Ploog, Structural and magnetic properties of epitaxial Fe_3Si/GaAs(001) hybrid structures, J. Vac. Sci. Technol. B, 22(4) (2004) 2073; https://doi.org/10.1116/1.1768528
[35] I. Arnay, J. López-Sánchez, E. Salas-Colera, F. Mompeán, A. del Campo, G. R. Castro and J. Rubio-Zuazo, The role of silicon oxide in the stabilization and magnetoresistance switching of Fe_3O_4/SiO_2/Si heterostructures, Materials Science and Engineering: B 271 (2021) 115248; https://doi.org/10.1016/j.mseb.2021.115248
[36] A. Berger, Magnetization reversal in granular thin films, Phys. B, 407 (9) (2011) 1322-1329 ; https://doi.org/10.1016/j.physb.2011.06.028